

Tuning magnetic anisotropy by interfacially engineering the oxygen coordination environment in a transition metal oxide

Daisuke Kan^{1*}, Ryotaro Aso¹, Riko Sato¹, Mitsutaka Haruta¹, Hiroki Kurata¹ and Yuichi Shimakawa^{1,2}

Strong correlations between electrons, spins and lattices—stemming from strong hybridization between transition metal *d* and oxygen *p* orbitals—are responsible for the functional properties of transition metal oxides. Artificial oxide heterostructures with chemically abrupt interfaces provide a platform for engineering bonding geometries that lead to emergent phenomena. Here we demonstrate the control of the oxygen coordination environment of the perovskite, SrRuO₃, by heterostructuring it with Ca_{0.5}Sr_{0.5}TiO₃ (0–4 monolayers thick) grown on a GdScO₃ substrate. We found that a Ru–O–Ti bond angle of the SrRuO₃/Ca_{0.5}Sr_{0.5}TiO₃ interface can be engineered by layer-by-layer control of the Ca_{0.5}Sr_{0.5}TiO₃ layer thickness, and that the engineered Ru–O–Ti bond angle not only stabilizes a Ru–O–Ru bond angle never seen in bulk SrRuO₃, but also tunes the magnetic anisotropy in the entire SrRuO₃ layer. The results demonstrate that interface engineering of the oxygen coordination environment allows one to control additional degrees of freedom in functional oxide heterostructures.

The oxygen coordination environments of the transition metals in transition metal oxides often underpin a wide variety of functional properties through crystal field splitting and magnetic interactions¹. Engineering the oxygen coordination environment in a given oxide, however, is rather difficult because it requires the modification of cation–oxygen bond lengths and angles that can be modified only by changing the temperature and applying chemical or physical pressure.

It has been demonstrated^{2–8} that artificial heterostructures and superlattices consisting of dissimilar oxides provide a good platform on which structural distortions associated with changes in metal–oxygen bonds, namely, the oxygen coordination environments, can be engineered. For perovskite oxides, bond distances and angles between a transition metal and oxygen are modified by oxygen displacements from the face-centred position. The modifications can be seen as oxygen octahedral distortions such as deformations and tilts (or rotations)^{9–12}. Although epitaxial strain due to lattice mismatch between films and substrates is widely used to modify the octahedral distortions and explore functional properties^{2–4,13}, strain-induced structural changes are rather complex^{12,14,15}, and controlling distortions by means of the strain is difficult. On the other hand, recent investigations have revealed that oxide films and superlattices even under fixed strain (the film's in-plane lattice parameters are fixed by the substrate lattice) accommodate various patterns of octahedral tilts, and as a result exhibit fascinating functional properties^{6,7,16–21}. This highlights that the oxygen in the heterostructures has degrees of freedom in its atomic position, which can be used in exploring functional properties. Furthermore, the octahedral tilts (or metal–oxygen bond angles) have been shown to be closely correlated with the interface structure characterized by corner-shared connections of two different oxygen octahedra^{7,22–24}. Interface engineering has thus been recognized as a promising route for controlling the octahedral tilts in the heterostructure. For modifying the interface structure, changing the chemical composition at the

interface, for example changing the substrate materials and introducing different composition buffer layers, is often used^{7,22,25,26}. This, however, also causes additional side effects and makes it difficult to understand how the degrees of freedom in the oxygen atomic position, especially at the heterointerface, influence structural and physical properties of entire heterostructures. Here we demonstrate that the layer-by-layer thickness control of a buffer layer at the interface allows engineering of the oxygen atomic position, namely oxygen coordination environments in heterostructures. We show that controlling the oxygen position at the heterointerface stabilizes the metallic and ferromagnetic SrRuO₃ (ref. 27; SRO, orthorhombic, $a_o = 5.57$ Å, $b_o = 5.53$ Å and $c_o = 7.85$ Å in bulk^{28,29}) perovskite layer with various Ru–O–Ru bond angles and magnetic anisotropy. (The subscript o denotes the orthorhombic perovskite notation.)

Recent experiments^{6,30–33} regarding structural distortions in perovskite oxide heterostructures have revealed that the octahedral tilt, which is associated with changes in the oxygen position, is modulated along the direction normal to the heterointerface (the out-of-plane direction) as a result of the accommodation of structural mismatch, and that the modulation decays within ~3 nm (corresponding to roughly 8 unit cells). This implies that the oxygen position at heterointerfaces can be controlled by inserting a buffer layer with the modulated octahedral tilts. In this study, we used an insulating and nonmagnetic Ca_{0.5}Sr_{0.5}TiO₃ (CSTO, orthorhombic, $a_o = 5.467$ Å, $b_o = 5.471$ Å, $c_o = 7.74$ Å in bulk³⁴) layer as a buffer layer because the modulated TiO₆ octahedral tilt has been indeed observed³¹ to persist up to 7 monolayers from the interface in CSTO layers epitaxially grown on GdScO₃ (GSO, orthorhombic, $a_o = 5.45$ Å, $b_o = 5.75$ Å, $c_o = 7.93$ Å in bulk^{35,36}) substrates that are paramagnetic insulators. Such modulated tilts have not been seen for ATiO₃ layers with divalent A-site cations whose ionic radius is relatively large, for example the BaTiO₃ layer on GSO, because the large A-site cations heavily suppress octahedral tilt propagation from the substrate³¹. We show that the oxygen

¹Institute for Chemical Research, Kyoto University, Uji, Kyoto 611-0011, Japan. ²Japan Science and Technology Agency, CREST, Uji, Kyoto 611-0011, Japan.
*e-mail: dkan@scl.kyoto-u.ac.jp

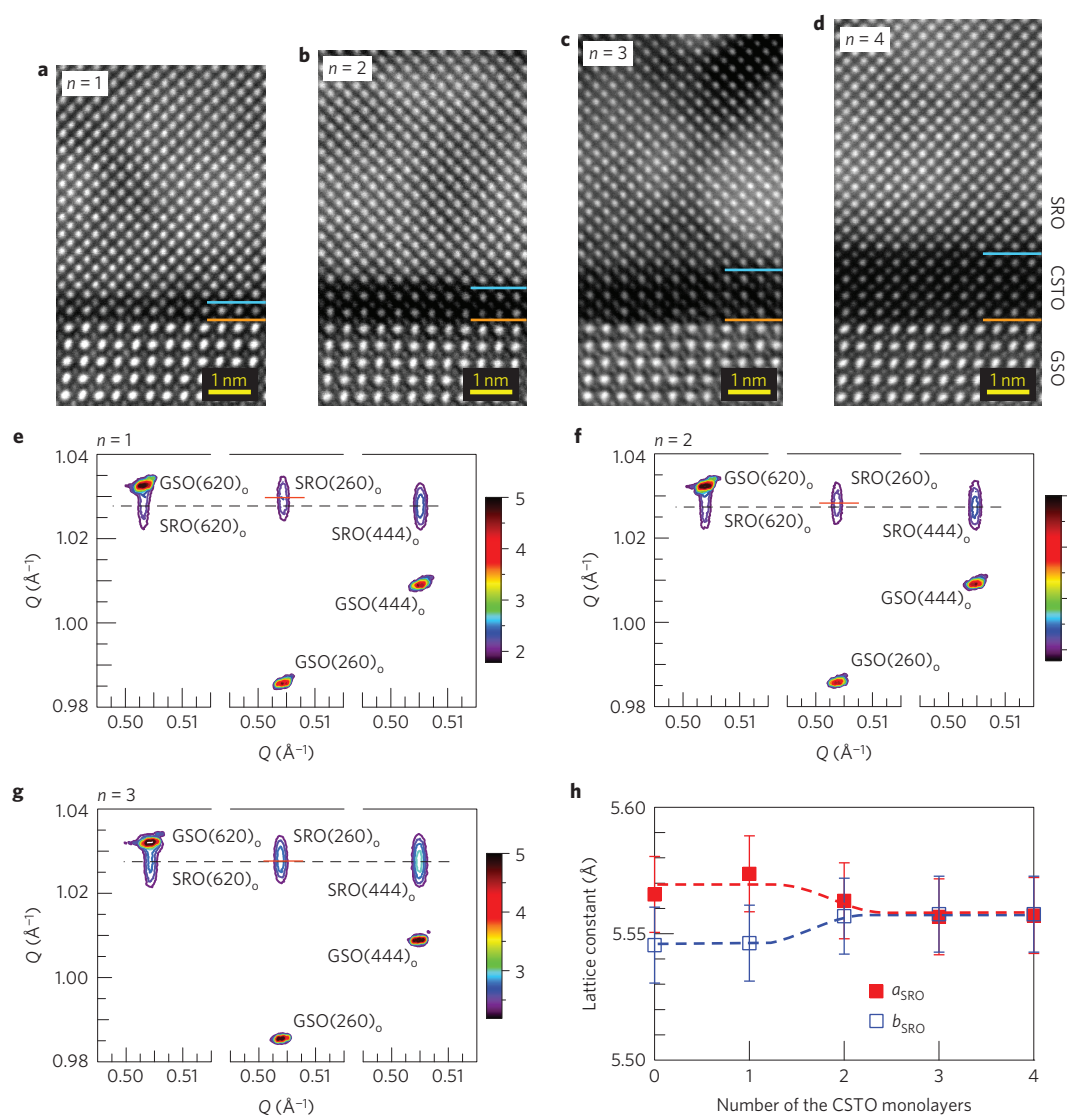


Figure 1 | Structural characterizations of SRO/CSTO_n/GSO heterostructures (n : number of monolayers in the CSTO layer). **a–d**, HAADF-STEM images for the $n=1$ (**a**), $n=2$ (**b**), $n=3$ (**c**) and $n=4$ (**d**) heterostructures. The images were taken along the [001]_o direction of the GSO substrate. The SRO/CSTO and CSTO/GSO interfaces are denoted by the blue and orange lines, respectively. **e–g**, X-ray reciprocal space mappings for the $n=1$ (**e**), $n=2$ (**f**) and $n=3$ (**g**) heterostructures. For each heterostructure, the mappings were taken around the (620)_o, (260)_o and (444)_o GSO reflections. The red and dashed black lines indicate the positions of the (260)_o and (444)_o SRO reflections, respectively. The colour code of the plotted intensities (in logarithmic scale) is given on the right next to each figure. **h**, Lattice constants of the SRO layer as a function of the CSTO layer thickness, revealing that the monoclinic SRO layer changes into the tetragonal form when the CSTO layer thickness is greater than three monolayers. The lattice constants were obtained from the (620)_o, (260)_o and (444)_o SRO reflection positions. The errors in the lattice constants were estimated from the uncertainty in the reflection position due to broadening of the reflection peaks.

coordination environment (or the Ru–O–Ru bond angle) in SRO can be interfacially controlled by inserting a very thin CSTO layer (0–4 monolayers thick) into the SRO/GSO heterointerface. Our aberration-corrected scanning transmission electron microscopy (STEM) observations reveal that the Ru–O–Ru bond angle in the entire SRO layer is controlled through the Ru–O–Ti bond angle, which is determined by the oxygen position at the SRO/CSTO interface. More importantly, the Ru–O–Ti bond angle (or the interfacial oxygen position) can be engineered by layer-by-layer control of the thickness of the CSTO buffer layer that stabilizes the oxygen coordination environment, a Ru–O–Ru bond angle not seen in bulk SRO. Our magneto-transport characterization of the SRO/CSTO/GSO heterostructures also shows that the Ru–O–Ti bond angle plays a decisive role in magnetic anisotropy with the uniaxial magnetic easy axis of the SRO layer, highlighting the

significant effect of the interfacially engineered oxygen coordination environment on the spin–orbit interaction of the SRO layer.

Control of oxygen coordination environment in SrRuO₃

SRO/CSTO_n/GSO heterostructures, where n (= 0–4) is the number of CSTO monolayers, were made using pulsed layer deposition (PLD)—See Methods. The CSTO layer was grown in the two-dimensional layer-by-layer growth mode and its thickness was controlled by *in-situ* monitoring the oscillation of the reflection high-energy electron diffraction (RHEED) spot intensity during the deposition. The thickness of the SRO layer in the heterostructure was fixed to be 10–12 nm. Figure 1a–d shows high-angle annular dark-field (HAADF) STEM images of the fabricated SRO/CSTO_n/GSO heterostructures. It is obvious that all the heterostructures are grown coherently, with no apparent

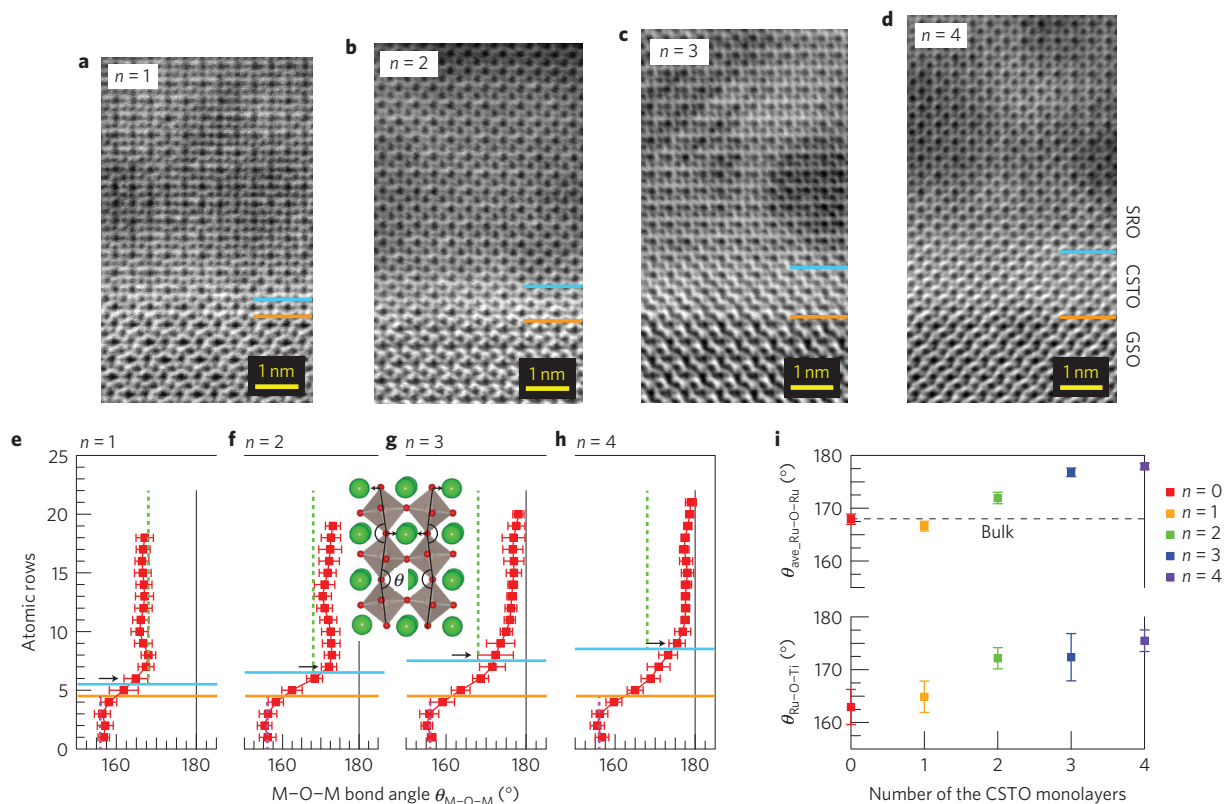


Figure 2 | Atomic-level characterization of the oxygen coordination environments (oxygen octahedral distortions) in SRO/CSTO_n/GSO heterostructures.

a–d, ABF-STEM images for the $n=1$ (**a**), $n=2$ (**b**), $n=3$ (**c**) and $n=4$ (**d**) heterostructures. The images were taken from the same region as the corresponding HAADF-STEM images in Fig. 1. The SRO/CSTO and CSTO/GSO interfaces are denoted by the blue and orange lines, respectively. **e–h**, M–O–M bond angle θ_{M-O-M} (M = Sc, Ti and Ru) as a function of the atomic position in the $n=1$ (**e**), $n=2$ (**f**), $n=3$ (**g**) and $n=4$ (**h**) heterostructures. The error bars correspond to the standard deviation of each θ_{M-O-M} . The definition of θ_{M-O-M} is given in the inset sketch. The in-plane oxygen displacement related to the octahedral tilt is also indicated with arrows in the schematics. We note that the bond angle θ_{M-O-M} used in this study corresponds to that projected on the (001)_o plane. The θ_{M-O-M} values for bulk SRO (168°, which corresponds to an oxygen displacement of 21 pm) and GSO (156° and 43 pm) are indicated by green and pink lines, respectively. $\theta_{Ti-O-Ti}$ for the bulk CSTO is 171°. The data points indicated by black arrows represent the Ru–O–Ti bond angle $\theta_{Ru-O-Ti}$. **i**, CSTO-layer-thickness dependence of $\theta_{ave_Ru-O-Ru}$ and $\theta_{Ru-O-Ti}$. The black dashed line represents $\theta_{Ru-O-Ru}$ for bulk SRO. The bond angle $\theta_{ave_Ru-O-Ru}$ of the SRO layer in each heterostructure (the upper panel) was determined by averaging over ten SRO unit cells from the top surface in the SRO/CSTO_n/GSO heterostructure (along the out-of-plane direction).

formation of misfit dislocations at the interface. The HAADF profiles (Supplementary Fig. 1) indicate that both CSTO/GSO and SRO/CSTO interfaces are sharp and that the interface layer is ScO₂ for CSTO/GSO and TiO₂ for SRO/CSTO, revealing that the B-site termination is maintained for each heterointerface. We also note that cation intermixing across the interface is negligibly small, as verified from elemental maps obtained by electron energy loss spectroscopy (Supplementary Fig. 2).

Figure 1e,f,g presents the X-ray reciprocal space mappings obtained for the heterostructures with $n=1$, 2 and 3, respectively. The mappings for the $n=0$ and 4 heterostructures, respectively, are essentially the same as those for the $n=1$ and 3 heterostructures. All reflections from the SRO layer are observed in the same position along the horizontal axis (in-plane direction), which is consistent with coherent growth of the entire heterostructure independent of the CSTO layer thickness (Fig. 1a–d). For the $n=1$ heterostructure (Fig. 1e), the (620)_o, (260)_o and (444)_o SRO reflections appear at different positions along the vertical axis (the out-of-plane direction), indicating that the SRO layer structure is monoclinic^{22,37,38}. For the $n=2$ heterostructure (Fig. 1f), the position difference of the (620)_o, (260)_o and (444)_o SRO reflections is smaller. The reflections for $n=3$ (Fig. 1g) are observed in the same position, indicating that the SRO layer has the tetragonal structure, which is the most stable for the SRO layer grown on the GSO substrate³⁷. In

Fig. 1h we plot the lattice constants of the SRO layer as a function of the CSTO layer thickness. The lattice constants are determined from the positions of the (620)_o, (260)_o and (444)_o reflections. The monoclinic SRO layer is stabilized in the heterostructures with the two-monolayer-thick or thinner CSTO ($n \leq 2$), whereas the tetragonal SRO is seen in the heterostructures with the three-monolayer-thick or thicker CSTO ($n \geq 3$). This dependence on the CSTO layer thickness of the structural transition in the SRO layer should be related to the changes in oxygen octahedral tilt associated with the oxygen displacement. We also note that the out-of-plane lattice constant determined from the position of the (220)_o SRO reflection in the X-ray $2\theta/\theta$ pattern coincides with that extracted from the HAADF-STEM image (Supplementary Fig. 3). This indicates that our local STEM measurements do provide essential information for the entire heterostructure.

We then performed cross-sectional annular bright-field (ABF) STEM observations of the SRO/CSTO_n/GSO ($n=1$ –4) heterostructures (Fig. 2a–d). The oxygen atomic columns are clearly visible in our ABF-STEM images, and the determination of their positions with sub-Å precision provides information on metal–oxygen bonds which is related to oxygen octahedral distortion and connection in the heterostructures. Figure 2e–h shows the variation of the M–O–M bond angle θ_{M-O-M} (M = Sc, Ti and Ru) as a function of the atomic position of the heterostructures

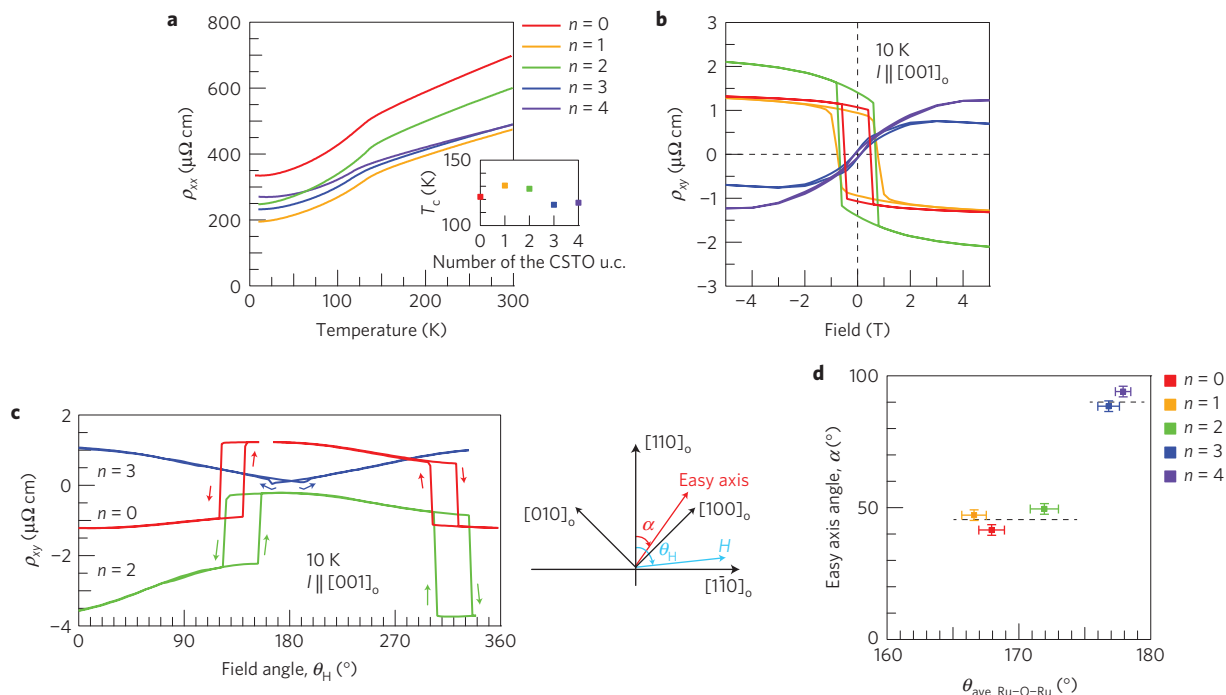


Figure 3 | Magneto-transport properties of the SRO/CSTO_n/GSO heterostructures. **a**, Temperature dependence of the longitudinal resistivity ρ_{xx} of the heterostructures ($n=0-4$). The inset shows the CSTO layer thickness dependence of the transition temperature T_c of the SRO layer. Both T_c and ρ_{xx} show no correlation with the CSTO layer thickness. **b**, Magnetic field dependence of the transverse Hall resistivity ρ_{xy} of the heterostructures ($n=0-4$). **c**, Field angle θ_H dependence of the Hall resistivity of the heterostructures ($n=0, 2$ and 3). A magnetic field of either 1.6 (for $n=0$ and 2) or 1 T (for $n=3$) was rotated in clockwise and anticlockwise directions within the $(001)_o$ plane of the heterostructure. The definition of the magnetic field angle θ_H , together with the magnetic easy axis angle α , is given in the sketch on the right. The data in **b** and **c** were obtained at 10 K. **d**, Magnetic easy axis angle α as a function of the Ru-O-Ru bond angle $\theta_{\text{ave,Ru-O-Ru}}$ in the SRO layer. The errors in α were estimated from the uncertainty in θ_H . We note that in the entire temperature range investigated here CSTO is insulating and nonmagnetic, and GSO is insulating and paramagnetic.

($n=1-4$). The variation of $\theta_{\text{M-O-M}}$ for the $n=0$ heterostructure is essentially the same as that for the $n=1$ heterostructure. The definition of $\theta_{\text{M-O-M}}$ is shown in the inset sketch to the figure. We note that $\theta_{\text{M-O-M}}$, which corresponds to the bond angle projected on the $(001)_o$ plane, represents the oxygen octahedral tilt resulting from the in-plane oxygen displacement. The experimental value of $\theta_{\text{M-O-M}}$ at each atomic position was determined by averaging over 18 unit cells along the in-plane direction. The Ru-O-Ru bond angle of the SRO layer in each heterostructure $\theta_{\text{ave,Ru-O-Ru}}$ was obtained by averaging over ten unit cells in the layer from the top surface (along the out-of-plane direction). It is seen that, for all the heterostructures, $\theta_{\text{Sc-O-Sc}}$ of $\sim 158^\circ$ in the GSO substrate region increases (the octahedral tilt decreases) towards the surface region and the behaviour is strongly dependent on the CSTO thickness n . For the $n=1$ heterostructure, the SRO layer maintains $\theta_{\text{ave,Ru-O-Ru}}$ as small as 167° , which is comparable to the bond angle for bulk SRO. With increasing n , $\theta_{\text{ave,Ru-O-Ru}}$ increases from $\sim 172^\circ$ for $n=2$ to $\sim 178^\circ$ for $n=4$. The increase in $\theta_{\text{ave,Ru-O-Ru}}$ with n is clearly seen in the upper panel of Fig. 2i. We also note that the bond angle in the top CSTO monolayer increases with increasing n . As a result, the Ru-O-Ti bond angle $\theta_{\text{Ru-O-Ti}}$ corresponding to the connection angle between the corner-shared TiO_6 and RuO_6 octahedra at the interface (arrowed in Fig. 2e-h) also increases as n increases, as shown in the lower panel in Fig. 2i. The observations indicate that $\theta_{\text{ave,Ru-O-Ru}}$, the oxygen coordination environment in the entire SRO layer, is engineered through $\theta_{\text{Ru-O-Ti}}$, controlled by the CSTO-layer-thickness-dependent modulation of the TiO_6 octahedral tilt. The smaller $\theta_{\text{Ru-O-Ti}}$ induced by the tilted TiO_6 octahedra leads to the smaller $\theta_{\text{ave,Ru-O-Ru}}$ (or the larger RuO_6 tilts) and stabilizes the monoclinic SRO layer. The modulated TiO_6 tilt decays in three-monolayer-thick or thicker CSTO, so the SRO layer in the

heterostructure with $n \geq 3$ has the tetragonal structure with the larger $\theta_{\text{ave,Ru-O-Ru}}$ (negligibly small octahedral tilt). Interestingly, an unusual $\theta_{\text{ave,Ru-O-Ru}}$, which has not been seen in bulk orthorhombic SRO, can be stabilized by controlling $\theta_{\text{Ru-O-Ti}}$ (the $n=2$ case). However, the bond angle controlled by $\theta_{\text{Ru-O-Ti}}$ always exceeds the bond angle of bulk SRO. This is probably because the size mismatch of the constituent A- and B-site cations also influences the bond angle according to the Goldschmidt tolerance factor^{11,39,40}. We also note that the SRO layer thickness at which the monoclinic-to-tetragonal structural transition takes place can be controlled by the CSTO layer thickness (Supplementary Fig. 3), indicating that tuning $\theta_{\text{Ru-O-Ti}}$, namely the interfacial oxygen position, is useful for structural phase control of the SRO layer.

Tuning magnetic anisotropy of SrRuO_3

Given that the RuO_6 octahedral distortion strongly influences the spin-orbit interaction in SRO (refs 41–44), the magnetic anisotropy of the SRO layer in SRO/CSTO_n/GSO can be controlled by means of $\theta_{\text{Ru-O-Ti}}$. Figure 3 shows the results of our magneto-transport characterization of the heterostructures ($n=0-4$). The temperature dependence of the longitudinal resistivity ρ_{xx} in Fig. 3a confirms that all heterostructures exhibit metallic conduction down to low temperatures and undergo a ferromagnetic transition around 120–130 K, as indicated by the hump in the ρ_{xx} versus temperature curves. In the inset of Fig. 3a, the transition temperature T_c is plotted as a function of the number n of CSTO monolayers. It is seen that both ρ_{xx} and T_c show no clear correlation with the CSTO layer thickness, which indicates that the $\theta_{\text{Ru-O-Ti}}$ -induced modulation of the Ru-O-Ru bond angle (or oxygen coordination environment) has little influence on the transport properties. The observed T_c is lower than the value of ~ 160 K for its bulk counterpart^{27,45}.

Because all the SRO layers are under tensile strain imposed by the GSO substrate, the observation might be an indication that the strain-induced change in the Ru–O bond distance strongly influences T_c . As shown in Fig. 3b,c, on the other hand, the anomalous part of the transverse Hall resistivity ρ_{xy} , which is associated with the magnetization M in the SRO layer, is strongly dependent on the CSTO layer thickness. Although the observed sign change of the anomalous Hall coefficient being dependent on the structure of the SRO layer suggests that there are changes in the Fermi surface of SRO, quantitative understanding of this phenomena will require further investigations, such as theoretical calculations. The observations in Fig. 3b,c reveal the strong impact of the controlled oxygen coordination environment ($\theta_{\text{ave_Ru-O-Ru}}$ or the RuO_6 octahedral distortions) on the spin–orbit interaction in the SRO layer. The field dependence of ρ_{xy} in Fig. 3b shows that, for the heterostructure with $n \leq 2$ in which the SRO layer includes the monoclinic distortions, the anomalous part of ρ_{xy} exhibits a square-shaped hysteresis, indicating that the magnetic moment has a component pointing in the out-of-plane direction. On the other hand, for the heterostructure with $n \geq 3$, in which the SRO layer structure is tetragonal with a large $\theta_{\text{Ru-O-Ru}}$, the anomalous part shows no (or negligibly small) hysteresis characteristics for the in-plane magnetization. The magnetic easy axis direction of the SRO layer was further determined from the field angle θ_H dependence of ρ_{xy} (Fig. 3c), which was taken by measuring ρ_{xy} under magnetic fields rotated in a complete revolution both in the clockwise and anticlockwise directions. We note that ρ_{xy} values of the $n = 1$ and 4 heterostructures, respectively, show essentially the same θ_H dependence as those for the $n = 0$ and 3 heterostructures. Given the strong uniaxial magnetic anisotropy of SRO, the magnetization does not follow the change in the magnetic field direction, and the magnetization reversal, which would occur when the angle between the magnetization and the field is greater than 90° , can be seen as jumps in ρ_{xy} . As expected, the results in Fig. 3c show that clear jumps in ρ_{xy} due to the magnetization reversal associated with the hysteresis in the clockwise and anticlockwise field rotations are observed every 180° in θ_H , confirming the uniaxial magnetic anisotropy of the SRO layer. The easy axis angle α of the SRO layer, which is determined from the centre position of the hysteresis in Fig. 3c, is plotted in Fig. 3d against the Ru–O–Ru bond angle $\theta_{\text{ave_Ru-O-Ru}}$ in the SRO layer. The magnetic moment for the heterostructure with the smaller $\theta_{\text{ave_Ru-O-Ru}}$ ($n \leq 2$) is tilted by $\sim 45^\circ$ with respect to the out-of-plane direction ($\alpha \sim 45^\circ$). This easy axis direction is basically the same as that for the bulk orthorhombic SRO (refs 42,43). On the other hand, the magnetic moment for the heterostructure with $\theta_{\text{ave_Ru-O-Ru}} \sim 180^\circ$ ($n \geq 3$) points in the $[110]_0$ (in-plane) direction (Supplementary Figs 4 and 5). We also note that the easy axis directions of all the heterostructures are independent of temperature (Supplementary Figs 4 and 5). The behaviour indicates that α changes in response to the monoclinic-to-tetragonal structural transition induced by $\theta_{\text{Ru-O-Ti}}$. The results demonstrate that the spin–orbit interaction of the SRO layer can be controlled by interfacially engineering the oxygen environment. It is interesting that the easy axis with $\alpha \sim 45^\circ$ comparable to the bulk is maintained even for the monoclinic SRO with $\theta_{\text{ave_Ru-O-Ru}}$ larger than its bulk counterpart (the $n = 2$ case). This indicates that the magnetic anisotropy in SRO is largely due to the magnetocrystalline effect, highlighting the importance of controlling the oxygen coordination environment that determines the compound's structural and electronic properties. Our results show that interfacial engineering of the oxygen position is useful for controlling the oxygen coordination environment in oxide heterostructures.

In summary, we demonstrate tuning of the magnetic anisotropy of SRO by interfacial control of the oxygen coordination environment in SRO. The atomic position of the oxygen shared by

the SRO and CSTO layers in the SRO/CSTO/GSO heterostructure is the controlling factor for the oxygen environment in the entire SRO layer, and can be engineered by layer-by-layer control of the CSTO layer thickness. Controlling the interfacial oxygen position can stabilize the SRO layer with a Ru–O–Ru bond angle not seen in bulk SRO. We also show that the interfacially engineered oxygen environment has a strong impact on the magnetic anisotropy through the spin–orbit interaction in the SRO layer. The results underscore the importance of oxygen coordination environments as a key factor determining the structural and physical properties of oxide heterostructures and show that interface engineering of the oxygen atomic position is useful in controlling the oxygen environment.

Note added in proof: After this manuscript was accepted we noticed the work by another group also reporting control of the oxide–interface properties by interface engineering⁴⁶.

Methods

Methods and any associated references are available in the [online version of the paper](#).

Received 27 April 2015; accepted 22 January 2016;
published online 7 March 2016

References

- Goodenough, J. B. *Magnetism and the Chemical Bond* (Interscience, 1963).
- Choi, K. J. *et al.* Enhancement of ferroelectricity in strained BaTiO_3 thin films. *Science* **306**, 1005–1009 (2004).
- Zeche, R. J. *et al.* A strain-driven morphotropic phase boundary in BiFeO_3 . *Science* **326**, 977–980 (2009).
- Lee, J. H. *et al.* A strong ferroelectric ferromagnet created by means of spin–lattice coupling. *Nature* **466**, 954–958 (2010).
- Bhattacharya, A. & May, S. J. Magnetic oxide heterostructures. *Annu. Rev. Mater. Res.* **44**, 65–90 (2014).
- May, S. J. *et al.* Control of octahedral rotations in $(\text{LaNiO}_3)_n/(\text{SrMnO}_3)_m$ superlattices. *Phys. Rev. B* **83**, 153411 (2011).
- Kim, Y.-M. *et al.* Interplay of octahedral tilts and polar order in BiFeO_3 films. *Adv. Mater.* **25**, 2497–2504 (2013).
- Kan, D., Aso, R., Kurata, H. & Shimakawa, Y. Research Update: Interface-engineered oxygen octahedral tilts in perovskite oxide heterostructures. *APL Mater.* **3**, 062302 (2015).
- Rondinelli, J. M., May, S. J. & Freeland, J. W. Control of octahedral connectivity in perovskite oxide heterostructures: an emerging route to multifunctional materials discovery. *MRS Bull.* **37**, 261–270 (2012).
- Glazer, A. M. The classification of tilted octahedra in perovskites. *Acta Crystallogr. B* **28**, 3384–3392 (1972).
- Woodward, P. M. Octahedral tilting in perovskites. I. Geometrical considerations. *Acta Crystallogr. B* **53**, 32–43 (1997).
- Rondinelli, J. M. & Spaldin, N. A. Structure and properties of functional oxide thin films: insights from electronic-structure calculations. *Adv. Mater.* **23**, 3363–3381 (2011).
- Schlom, D. G. *et al.* Strain tuning of ferroelectric thin films. *Annu. Rev. Mater. Res.* **37**, 589–626 (2007).
- Vailionis, A. *et al.* Misfit strain accommodation in epitaxial ABO_3 perovskites: lattice rotations and lattice modulations. *Phys. Rev. B* **83**, 064101 (2011).
- Rondinelli, J. M. & Coh, S. Large isosymmetric reorientation of oxygen octahedra rotation axes in epitaxially strained perovskites. *Phys. Rev. Lett.* **106**, 235502 (2011).
- Choi, K. J. *et al.* Phase-transition temperatures of strained single-crystal SrRuO_3 thin films. *Adv. Mater.* **22**, 759–762 (2010).
- Moon, E. J. *et al.* Spatial control of functional properties via octahedral modulations in complex oxide superlattices. *Nature Commun.* **5**, 5710 (2014).
- Bousquet, E. *et al.* Improper ferroelectricity in perovskite oxide artificial superlattices. *Nature* **452**, 732–736 (2008).
- Chang, S. H. *et al.* Thickness-dependent structural phase transition of strained SrRuO_3 ultrathin films: the role of octahedral tilt. *Phys. Rev. B* **84**, 104101 (2011).
- Biegalski, M. D. *et al.* Interrelation between structure–magnetic properties in $\text{La}_{0.5}\text{Sr}_{0.5}\text{CoO}_3$. *Adv. Mater. Interfaces* **1**, 1400203 (2014).

21. Lu, W., Yang, P., Song, W. D., Chow, G. M. & Chen, J. S. Control of oxygen octahedral rotations and physical properties in SrRuO₃ films. *Phys. Rev. B* **88**, 214115 (2013).
22. Kan, D., Aso, R., Kurata, H. & Shimakawa, Y. Phase control of a perovskite transition-metal oxide through oxygen displacement at the heterointerface. *Dalton Trans.* **44**, 10594–10607 (2015).
23. Aso, R., Kan, D., Shimakawa, Y. & Kurata, H. Control of structural distortions in transition-metal oxide films through oxygen displacement at the heterointerface. *Adv. Funct. Mater.* **24**, 5177–5184 (2014).
24. Moon, E. J. *et al.* Effect of interfacial octahedral behavior in ultrathin manganite films. *Nano Lett.* **2014**, 2509–2514 (2014).
25. Jang, H. W. *et al.* Metallic and insulating oxide interfaces controlled by electronic correlations. *Science* **331**, 886–889 (2011).
26. Chen, Z. H., Damodaran, A. R., Xu, R., Lee, S. & Martin, L. W. Effect of “symmetry mismatch” on the domain structure of rhombohedral BiFeO₃ thin films. *Appl. Phys. Lett.* **104**, 182908 (2014).
27. Koster, G. *et al.* Structure, physical properties, and applications of SrRuO₃ thin films. *Rev. Mod. Phys.* **84**, 253–298 (2012).
28. Jones, C. W., Battle, P. D., Lightfoot, P. & Harrison, W. T. A. The structure of SrRuO₃ by time-of-flight neutron powder diffraction. *Acta Crystallogr. C* **45**, 365–367 (1989).
29. Kennedy, B. J. & Hunter, B. A. High-temperature phases of SrRuO₃. *Phys. Rev. B* **58**, 653–658 (1998).
30. Borisevich, A. Y. *et al.* Suppression of octahedral tilts and associated changes in electronic properties at epitaxial oxide heterostructure interfaces. *Phys. Rev. Lett.* **105**, 087204 (2010).
31. Aso, R., Kan, D., Shimakawa, Y. & Kurata, H. Octahedral tilt propagation controlled by A-site cation size at perovskite oxide heterointerfaces. *Cryst. Growth Design* **14**, 2128–2132 (2014).
32. Jia, C. L. *et al.* Oxygen octahedron reconstruction in the SrTiO₃/LaAlO₃ heterointerfaces investigated using aberration-corrected ultrahigh-resolution transmission electron microscopy. *Phys. Rev. B* **79**, 081405 (2009).
33. Fister, T. T. *et al.* Octahedral rotations in strained LaAlO₃/SrTiO₃ (001) heterostructures. *APL Mater.* **2**, 021102 (2014).
34. Yamanaka, T., Hirai, N. & Komatsu, Y. Structure change of Ca_{1-x}Sr_xTiO₃ perovskite with composition and pressure. *Am. Mineral.* **87**, 1183–1189 (2002).
35. Schubert, J. *et al.* Structural and optical properties of epitaxial BaTiO₃ thin films grown on GdScO₃ (110). *Appl. Phys. Lett.* **82**, 3460 (2003).
36. Biegalski, M. D. *et al.* Thermal expansion of the new perovskite substrates DyScO₃ and GdScO₃. *J. Mater. Res.* **20**, 952–958 (2011).
37. Kan, D., Aso, R., Kurata, H. & Shimakawa, Y. Thickness-dependent structure–property relationships in strained (110) SrRuO₃ thin films. *Adv. Funct. Mater.* **23**, 1129–1136 (2013).
38. Vailionis, A., Siemons, W. & Koster, G. Room temperature epitaxial stabilization of a tetragonal phase in ARuO₃ (A = Ca and Sr) thin films. *Appl. Phys. Lett.* **93**, 051909 (2008).
39. Goodenough, J. B. Electronic and ionic transport properties and other physical aspects of perovskites. *Rep. Prog. Phys.* **67**, 1915–1993 (2004).
40. Goldschmidt, V. M. Die Gesetze der Krystallochemie. *Naturwissenschaften* **14**, 477–485 (1926).
41. Kanbayasi, A. Magnetic properties of SrRuO₃ single crystal. *J. Phys. Soc. Jpn* **41**, 1876–1878 (1976).
42. Kanbayasi, A. Magnetic properties of SrRuO₃ single crystal. II. *J. Phys. Soc. Jpn* **44**, 89–95 (1978).
43. Cao, G., McCall, S., Shepard, M., Crow, J. E. & Guertin, R. P. Thermal, magnetic, and transport properties of single-crystal Sr_{1-x}Ca_xRuO₃ (0 ≤ x ≤ 1.0). *Phys. Rev. B* **56**, 321–329 (1997).
44. Kats, Y., Genish, I., Klein, L., Reiner, J. W. & Beasley, M. R. Large anisotropy in the paramagnetic susceptibility of SrRuO₃ films. *Phys. Rev. B* **71**, 100403 (2005).
45. Allen, P. B. *et al.* Transport properties, thermodynamic properties, and electronic structure of SrRuO₃. *Phys. Rev. B* **53**, 4393–4398 (1996).
46. Liao, Z. *et al.* Controlled lateral anisotropy in correlated manganite heterostructures by interface-engineered oxygen octahedral coupling. *Nature Mater.* <http://dx.doi.org/10.1038/nmat4579> (2016).

Acknowledgements

This work was partially supported by the Core Research for Evolutional Science and Technology (CREST) programme of the Japan Science and Technology Agency. The work was also supported by a grant for the Joint Project of Chemical Synthesis Core Research Institutions from the Ministry of Education, Culture, Sports, Science and Technology of Japan.

Author contributions

D.K. conceived the idea and initiated the project. D.K. and R.S. fabricated the samples and performed X-ray structural characterization and transport measurements. R.A. and M.H. collected and analysed the STEM data. H.K. and Y.S. supervised the project. All authors discussed the experimental data and co-wrote the manuscript.

Additional information

Supplementary information is available in the [online version of the paper](#). Reprints and permissions information is available online at www.nature.com/reprints. Correspondence and requests for materials should be addressed to D.K.

Competing financial interests

The authors declare no competing financial interests.

Methods

Fabrication. The SrRuO_3 (SRO)/ $\text{Ca}_{0.5}\text{Sr}_{0.5}\text{TiO}_3$ (CSTO)/ GdScO_3 (GSO) heterostructures were fabricated by epitaxially growing SRO (orthorhombic, $a_o = 5.57 \text{ \AA}$, $b_o = 5.53 \text{ \AA}$, and $c_o = 7.85 \text{ \AA}$ in bulk^{28,29}) and CSTO (orthorhombic, $a_o = 5.467 \text{ \AA}$, $b_o = 5.471 \text{ \AA}$, $c_o = 7.74 \text{ \AA}$ in bulk³⁴) layers on $(110)_o$ GSO (orthorhombic, $a_o = 5.45 \text{ \AA}$, $b_o = 5.75 \text{ \AA}$, $c_o = 7.93 \text{ \AA}$ in bulk^{35,36}) substrates by pulsed laser deposition (PLD). Based on the lattice mismatch (calculated from the pseudo-cubic lattice constants) between SRO, CSTO and GSO, the SRO and CSTO layers are subjected to $\sim 1.0\%$ and $\sim 2.5\%$ tensile strain, respectively. The CSTO layer was deposited at a substrate temperature of 700°C and an oxygen partial pressure of 1×10^{-5} torr. The number of monolayers in the CSTO layer was controlled by *in-situ* monitoring oscillation of the reflection high-energy electron diffraction (RHEED) spot intensity. The CSTO deposition was followed, without breaking the vacuum of the PLD chamber, by deposition of the SRO layer (10–12 nm thick) at the same temperature and an oxygen partial pressure of 100 mtorr.

Characterization. Structural characterization of the fabricated heterostructures was performed with conventional 4-circle X-ray diffraction (X'pert MRD, PANalytical) and cross-sectional HAADF- and ABF-STEM observations. The thickness of the SRO layer was determined from the period of the thickness fringes seen in the X-ray $2\theta/\theta$ profiles for the fabricated SRO/CSTO/GSO heterostructures (typical X-ray $2\theta/\theta$ profiles are provided in Supplementary Fig. 3). Details of the STEM observations and their analysis can be found in our previous reports⁴⁷. For the evaluation of the magneto-transport properties, the heterostructures were patterned into 50- μm -wide Hall bars by conventional photolithography and Ar ion milling. The longitudinal and transverse Hall resistivities were measured in a conventional four-probe configuration with a Physical Property Measurement System (PPMS, Quantum Design) equipped with a sample rotator.

References

47. Aso, R., Kan, D., Shimakawa, Y. & Kurata, H. Atomic level observation of octahedral distortions at the perovskite oxide heterointerface. *Sci. Rep.* **3**, 2214 (2013).